



<http://www.diva-portal.org>

This is the published version of a paper published in *Talanta: The International Journal of Pure and Applied Analytical Chemistry*.

Citation for the original published paper (version of record):

An, S., Reza, S., Norlin, B., Fröjd, C., Thungström, G. (2021)

Signal-to-noise ratio optimization in X-ray fluorescence spectrometry for chromium contamination analysis

Talanta: The International Journal of Pure and Applied Analytical Chemistry, 230: 122236

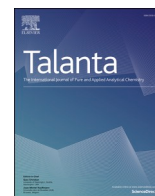
<https://doi.org/10.1016/j.talanta.2021.122236>

Access to the published version may require subscription.

N.B. When citing this work, cite the original published paper.

Permanent link to this version:

<http://urn.kb.se/resolve?urn=urn:nbn:se:hig:diva-35554>



Signal-to-noise ratio optimization in X-ray fluorescence spectrometry for chromium contamination analysis

Siwen An^{a,*}, Salim Reza^b, Börje Norlin^a, Christer Fröjdh^a, Göran Thungström^a

^a Department of Electronics design, Mid Sweden University, Sundsvall, Sweden

^b Department of Electrical Engineering, Mathematics and Science, University of Gävle, Gävle, Sweden

ARTICLE INFO

Keywords:

Chromium
Environmental monitoring
Hazardous materials
Limit of quantitation (LOQ)
Waste management
X-ray fluorescence analysis (XRF)

ABSTRACT

In most cases, direct X-ray fluorescence (XRF) analysis of solutions entails technical difficulties due to a high X-ray scattering background resulting in a spectrum with a poor signal-to-noise ratio (SNR). Key factors that determine the sensitivity of the method are the energy resolution of the detector and the amount of scattered radiation in the energy range of interest. Limiting the width of the primary spectrum by the use of secondary targets, or filters, can greatly improve the sensitivity for specific portions of the spectrum. This paper demonstrates a potential method for SNR optimization in direct XRF analysis of chromium (Cr) contamination. The suggested method requires minimal sample preparation and achieves higher sensitivity compared to existing direct XRF analysis. Two states of samples, fly ash and leachate from municipal solid waste incineration, were investigated. The effects of filter material, its absorption edge and filter thickness were analyzed using the combination of Monte Carlo N-Particle (MCNP) code and energy-dispersive XRF spectrometry. The applied filter removes primary photons with energies interfering with fluorescence photons from the element of interest, thus results in lower background scattering in the spectrum. The SNR of Cr peak increases with filter thickness and reaches a saturation value when further increased thickness only increases the measurement time. Measurements and simulations show that a Cu filter with a thickness between 100 μm and 140 μm is optimal for detecting Cr by taking into account both the SNR and the exposure time. With direct XRF analysis for solutions, the limit of quantitation (LOQ) of the achieved system was 0.32 mg/L for Cr, which is well below the allowed standard limitation for landfills in Sweden. This work shows that XRF can gain enough sensitivity for direct monitoring to certify that the Cr content in leachate is below environmental limits.

1. Introduction

Incineration of municipal solid waste (MSW) is an efficient method in waste management, because of the high energy recovery and the reduction of volume and weight of the waste. Incineration, however, generates fly ash containing several toxic elements. Waste incineration ashes are dumped either directly in controlled sites for toxic materials or after treatment in open landfill sites [1]. In the latter case, leachate water might be generated due to rainwater. The leachate washes out or extracts toxic components, minerals and other materials while percolating through wastes. Together with many hazardous materials including Chromium (Cr), the contents from the waste incineration can be washed out and cause a significant threat to surface water and groundwater [2]. Cr is a major pollutant for the environment and exists mainly in two different oxidation states, Cr (III) and Cr (VI). The former

is essential to normal carbohydrate, lipid, and protein metabolism, while the latter is a major pollutant of the environment. In general, Cr (VI) compounds are more toxic than the Cr (III) compounds [3]. Cr (VI) is quite mobile in soils due to its charge repulsion and solubility [4]. Moreover, it can induce carcinogenesis because of its ability to cross biological membranes easily and react with protein components and nucleic acids inside the cell [5]. In the natural environment, the presence of oxygen or manganese dioxide can oxidize Cr (III) to Cr (VI). According to Amita D Apte [6], the conversion rate has been increased up to 50% when heated in the presence of oxygen at temperatures of 200 °C–300 °C. The major environmental concern in relation to the short- and long-term impacts of MSW residue disposal is the risk of leaching and subsequent release of potentially harmful substances into the environment. It thus becomes essential to monitor the total Cr content in the ash and the leachate routinely.

* Corresponding author. Mid Sweden University, Department of Electronics design, Sundsvall, SE-85170, Sweden.

E-mail address: siwen.an@miun.se (S. An).

<https://doi.org/10.1016/j.talanta.2021.122236>

Received 20 August 2020; Received in revised form 14 February 2021; Accepted 17 February 2021

Available online 22 February 2021

0039-9140/© 2021 The Authors. Published by Elsevier B.V. This is an open access article under the CC BY license (<http://creativecommons.org/licenses/by/4.0/>).

Table 1

Characteristic X-ray emissions from Cr and relative intensities of K-, L-shell lines. The strongest line in each shell is assigned to the relative intensity of 100.

Emission line	Fluorescence (keV)	Relative intensity
$K\alpha_1$	5.415	100
$K\alpha_2$	5.406	50
$K\beta_{1,3}$	5.947	15
$L\alpha_{1,2}$	0.573	111
$L\beta_1$	0.583	79
$L\gamma_1$	0.500	17

Techniques of sample analysis play an important role in environmental studies. Wide ranges of analytical techniques are available for the determination of Cr; namely inductively coupled plasma atomic emission spectrometry (ICP-AES), inductively coupled plasma mass spectrometry (ICP-MS) [7], and atomic absorption spectroscopy (AAS) [8]. Most of these methods need a complicated sample preparation process, such as sample dissolution or digestion that might introduce a number of additional chemicals. Beyond these techniques, X-ray fluorescence (XRF) technique may also be used for the determination and analysis of Cr in industrial and environmental measurements [9–11]. The desired feature of the XRF technique for this application is the capability of direct analysis. The XRF instrument must be precisely calibrated in order to ensure that the results are accurate. In most commercial XRF instruments, the calibration is valid only for one specific type of solid-state samples, such as mining, soil, alloy and plastic, etc. Depending on the acquisition time, the specific element and the sample matrix, a typical commercial XRF spectrometer has the limit of detection range from 100% down to ppm and in some cases sub-ppm levels [12,13]. However, XRF is normally not considered to be suitable for the measurement of dissolved components in aqueous samples due to the high scattered background from the water surface [14,15]. The main disadvantage of XRF technique is the insufficient sensitivity for some important pollutants elements and pre-concentration is often necessary for trace elements analysis when detecting liquid samples [16]. Previous researchers have shown that after a solid-phase extraction process, matrix effects were eliminated and concentrations of Cr in the range $\mu\text{g/L}$ was achieved in aqueous samples such as drinking water [17]. Unfortunately, the pre-concentration process is tedious and difficult for an on-site environmental monitoring system with rapid response.

The aim of this study is to optimize direct XRF analysis for Cr contamination in fly ash and leachate samples with relatively low concentrations by using an optimal primary beam filter. The performance of two filter materials with several thicknesses, Copper (Cu) and Germanium (Ge), were investigated using the combination of Monte Carlo N-Particle (MCNP) code [18] and energy-dispersive XRF laboratory experiments. This study verifies that the MCNP simulator is an efficient tool for filter optimization providing good agreement with measurements. The present work illustrates that it is possible to determine an optimal filter thickness, which reduces the scattered background noise but also keeps the X-ray source intensity rate at a useful level. We demonstrate that by increasing the thickness of a primary X-ray beam filter, the signal-to-noise ratio (SNR) in XRF measurements is optimized to reach a saturation value for both filter materials. The limit of quantitation (LOQ) was determined with the usage of SNR calculation for making objective analytical decisions in XRF quantitative analysis. In addition, the matrix effects in samples containing two elements, Fe–Cr, was investigated using MCNP simulation. The main advantage of the suggested XRF technique is the capability to analyze the elemental composition directly even at concentrations slightly below the environmental limit.

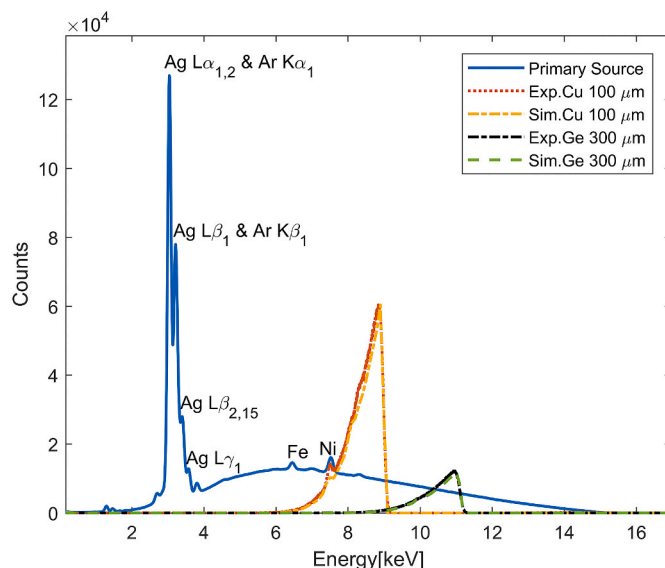


Fig. 1. Primary source spectrum and filtered spectra with a 100 μm Cu filter and a 300 μm Ge filter. The MCNP simulation data is normalized in order to compare with the experiment.

2. XRF theory

2.1. Characteristic emission lines of Cr

XRF is the emission of characteristic (or fluorescent) X-rays from a material that has been excited by being bombarded with high-energy X-rays. The intensity of the fluorescence depends on the fluorescence yield ω , which is defined as the ratio of the number of photons emitted to the number of photons absorbed in each shell. For Cr, the fluorescence yield ω_K of the K-shell is 28.8%, while the yield ω_L of the L-shell is 0.071%–0.37%. The intensity of the fluorescence lines are governed by the fluorescence yield, and distributed on several lines with varying intensities within each shell. The relative intensity for fluorescence photon energy lines of Cr is shown in Table 1 [19]. Each line corresponds to a transition between two different shells. The spectrum from X-ray fluorescence contains characteristic lines which can be used to identify the material. For many instruments, the $K\alpha_1$ and $K\alpha_2$ lines of Cr will merge into one line since the photon energy is too close to separate with the spectral resolution in the energy-dispersive spectrometer. Thus, this merged $K\alpha$ -line is the most efficient line to detect in a Cr monitoring application due to the high fluorescence yield. Ideally, the intensity of an element in a sample should be a linear function of its concentration within a certain range. However, the experimental data might show deviation due to the presence of other elements. This is defined as matrix effect, and it can have considerable effects on the quality of the results.

2.2. Primary radiation and filtered X-ray spectra

The typical source spectrum of an X-ray tube consists of a continuous spectrum of X-rays, with additional sharp peaks at certain energies. The continuous spectrum is due to bremsstrahlung of the incident electron beam, while the sharp peaks are characteristic X-rays associated with the element in the source target. Compton scattering of photons from the X-ray tube will occur in the sample, this will contribute to background noise, which will significantly reduce the sensitivity of the detecting system. Thus, the effect of the primary X-ray radiation must be considered in XRF measurements. Fig. 1 (Primary source) shows the primary radiation from an X-ray tube equipped with a Silver (Ag) anode target at 15 kV. The two significant peaks in the primary X-ray source spectrum are 2.98 keV and 3.15 keV originating from the L-lines characteristic X-rays of the Ag anode in the X-ray tube. The strong L-line characteristic X-

rays of the Ag in the source excites Si fluorescence photons that escape from the detector, thus, the reabsorb photon energy is the Ag photon energy minus the Si fluorescence energy of 1.74 keV resulting in two escape peaks at 1.24 keV and 1.41 keV. The peaks at 6.41 keV and 7.48 keV come from Iron (Fe) and Nickel (Ni) separately, materials presented in the detector and source housing. The continuous spectrum of the X-ray tube ranges from low energies up to the tube voltage, 1 keV–15 keV. As a result, a high background occurs at 5.41 keV, which will decrease the sensitivity for the $K\alpha$ peak of Cr.

In XRF analyses, only photons with energies above the absorption edge of the element of interest will generate fluorescence signal. Energies below the K-edge of Cr will hence only contribute to background noise and lower down the SNR. The main function of the primary source filter is to pass photons with energy high enough to excite the K-shell of Cr, and in the same time block energies that interfere with the fluorescence lines to be measured [20]. Photons with energies just above a fluorescence line might interfere with the Cr signal determination if they lose energy due to Compton scattering in air or in the surroundings. When optimizing the primary source filter, the probability of single and multiple Compton scattering must be considered, thereby the presence of scattered photons with energies around 5.41 keV ($K\alpha$ of Cr) is minimal. Fig. 1 gives an example of the filtered spectra from two metal filters, a 100 μm Cu filter and a 300 μm Ge filter. In the MCNP simulation, we use the measured source spectrum (Fig. 1 Primary source) as the input source with tabulated energy distribution in the simulation. The agreement between the experiment and simulation validated that the MCNP model can be used for simulation of K-edge transmission of a material. By applying a 100 μm Cu filter, it mainly allows photons from the X-ray source with energies mainly between 6 keV and 9 keV to pass through it, while a 300 μm Ge filter has a higher energy range from 8 keV to 11 keV. Moreover, the filtered X-ray intensity after a 100 μm Cu filter is approximately three times higher than after a 300 μm Ge filter. The filtered spectra act as a nearly monochromatic source that will excite the sample but not interfere with the fluorescence photons from the element of interest. The Ni peak at 7.48 keV, which is caused by the instrument material, transmit the Cu filter and remains in the filtered spectra. It should be noted that if the X-ray voltage is set too high, photons with high energies will penetrate the filter, thus resulting in a high energy 'tail'. Similarly, this phenomenon exists when the filter is too thin (which can be observed for the energy part above 9 keV in Fig. 3). However, the high energy 'tail' is far away from 5.41 keV and it also contributes to the generation of Cr fluorescent photons. Comparing with the primary spectrum, both filters remove the scattered photons around 5.41 keV, resulting in a lower background signal.

3. Methods

3.1. Sample preparation

Two sample forms, solid (fly ash) and liquid (leachate), were collected from the city incineration plant in Sundsvall and analyzed in this study. The ash sample was roughly ground to fine grains. Color and grain size of the solid ash sample looks homogeneous upon visual inspection. The thickness of the ash sample is approximately 1.5 cm. For liquid sample calibrations, the measurement system has been used to record the fluorescent photons from prepared samples with Cr concentrations of 3.9, 1.9, 1, 0.5, 0.25 mg/L, purified water (Milli-Q integral water purification system) and leachate sample. These calibration standard samples are made of $\text{Cr}(\text{NO}_3)_3 \cdot 9\text{H}_2\text{O}$. The tested amount of all liquid samples is 80 mL per sample in the experiments. All liquid samples are regarded as homogeneous samples.

3.2. MCNP simulation for liquid samples

The latest version MCNP 6.2 was used in this study. This version can separate the L-lines of the characteristic X-ray emissions with the

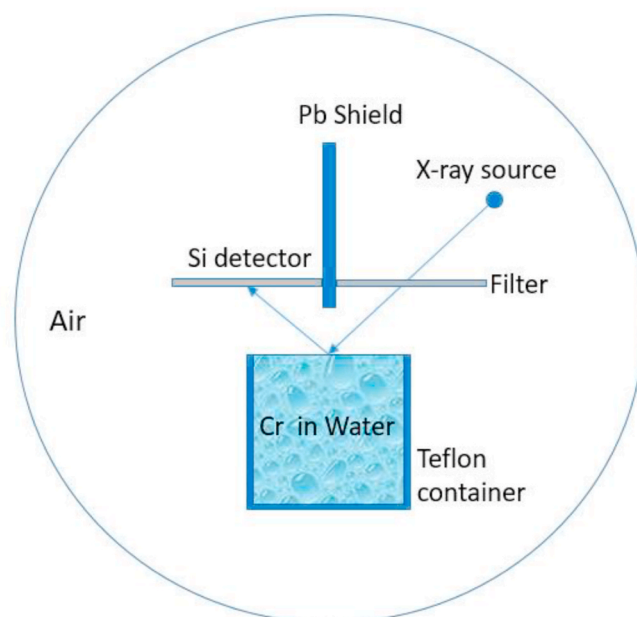


Fig. 2. Geometry model of the XRF setup used for MCNP simulation. The filter removes low energies from the source spectrum that interferes the fluorescence lines from the sample.

electron-photon relaxation library (EPRDATA14), which is not available in earlier versions. Modelling of separated L-lines is necessary when simulating environmental XRF measurements, since Lead (Pb), Mercury (Hg) and other heavy elements can be present in regular fly ash samples. However, the simulations presented in this study focus on Cr, and the L-lines from Cr will not be recorded due to the strong air absorption for low energy photons.

The geometrical model of the XRF detection system in the MCNP simulation is shown in Fig. 2. The procedure starts with the definition of an X-ray source (defined as a point source here) emitting X-rays towards the center of the top surface of the sample. By considering the bremsstrahlung effect of the incident X-ray spectrum, a laboratory-measured MOXTEK X-ray tube spectrum with tube voltage at 15 kV is implemented in this simulation as the input source. The atmosphere in the simulation is air, which contains approximately 78% Nitrogen (N), 21% Oxygen (O) and 0.9% Argon (Ar). The primary filter is placed between the source and the sample to limit the width of the primary exciting spectrum. A variety of filters (copper and germanium) with thickness 25 μm , 50 μm , 75 μm , 100 μm , 125 μm , 150 μm , 175 μm and 200 μm are simulated and compared. It should be noted that the filter thickness is defined as the cross-section of the filter plate since the angle of incidence is 45° in the simulation. The modelled material composition of the liquid sample is simplified, which mainly consists of H_2O and with an added part of Cr with varying mass concentrations in a 1 cm^3 cubic Teflon container. We assume that the density of all liquid samples is 1 g/cm^3 because the mass weight of Cr can be ignored. The sample is irradiated by the filtered spectrum. Subsequently, the fluorescence X-rays coming from the focal spot on the sample are absorbed and recorded by a Silicon (Si) detector. Table 2 lists the MCNP simulation parameters used in this study.

3.3. XRF measurements setup

The energy dispersive XRF measurements is performed using a MOXTEK MAGPRO X-ray source (5 kV–60 kV, 12 W) and a silicon drift spectrometer (Amptek X-123SDD) in the X-ray lab at Mid Sweden University. The material of the X-ray tube anode target is Ag and the typical focal spot size is about 400 μm [21]. The spectral resolution in terms of

Table 2
MCNP parameters used for simulation.

Item	Parameters	Setting
Input source from measured spectrum of MOXTEK MAGPRO	Beam energy (kVp)	15
	Source current (μA)	2
	Measurement distance (cm)	2.8
	Acquisition time (min)	42
Filter foil	Filter material	Cu/Ge
	Filter thickness Cu (μm)	25, 50, 75, 100, 125, 150, 175, 200
	Filter thickness Ge (μm)	25, 50, 75, 100, 125, 150, 175, 200, 300
	Detector material	Silicon
Spectrometer	Detector size	1 cm × 1 cm (Square)
	Thickness (μm)	500
	Energy bin width (eV)	100
	Type of particles	Photons and electrons
Simulation setting	Number of particles (NPS)	60000000
	Version	MCNP 6.2
	Electron-photon relaxation library	EPRDATA14

Table 3
Instrumental configurations and parameters used for acquisition.

Item	Parameters	Ash	Cr in liquid
X-ray source (MOXTEK MAGPRO)	Beam energy (kVp)	15	15
	Source current (μA)	700	300/800
	Acquisition time	10 min	2 h
Filter foil	Filter material	Cu	Cu/Ge
	Filter thickness (μm)	130	100/300
Spectrometer (Amptek X-123SDD)	Detector material	Silicon drift detector	
	Detector size	25 mm ² (Circle)	
	Thickness (μm)	500	
	Energy resolution (eV)	125–140	

full width at half maximum (FWHM) of the spectrometer at 5.9 keV is 125 eV–140 eV [22]. The angle between incident primary radiation and the sample is approximately 60° and the angle between sample and detector is approximately 50°. The difference incident angle of the experiment and the simulation will cause a slight shift of continues X-ray spectrum due to the Compton scattering. However, the energy shift of the scattered photon overlapping with the fluorescence signal are insignificant for low energies. Two Cu sleeves were mounted at the end of the X-ray tube and the spectrometer, respectively, to shield the detector from both scattered radiation and primary radiation from the X-ray source. It should be noted that iron-chromium alloy, also called ferrochrome, is widely used in the production of stainless steel. The Cr from the stainless steel mounting pillars in the setup interferes the Cr detection measurements. By covering the stainless steel pillars with a Cu shield, the Cr signal coming from the surroundings is significantly reduced. Table 3 displays the instrumental configurations used to generate the data that were used for the calculations in this study.

3.4. Signal-to-noise ratio

When evaluating an XRF spectrum, the signal-to-noise ratio (SNR) provides objective determination in peak searching. The peaks in the XRF measurements follow a nearly Gaussian distribution because of the imperfect resolution of semiconductor detectors, and the net peak is equal to the difference between the total count and the background count in the region of interest. Therefore, the total counts (TC) and background counts (BG) for a peak of interest must be obtained to calculate the SNR in an XRF spectrum [23]. The total counts, which include signal and background, through the energy range of the peak of

interest are calculated as:

$$TC = \sum_{k=m}^n P_c \quad (1)$$

where, m is the first channel number of the peak of interest; n is the last channel number of the peak; P_c is the photon counts for each channel. The background counts are computed by multiplying the number of channels in the peak of interest by the average of pre-peak and post-peak background:

$$BG = (n - m + 1) * \left(\sum_{k=m-a}^{m-1} P_c + \sum_{k=n+1}^{n+a} P_c \right) / 2a \quad (2)$$

where, a is the number of the channels of the pre-peak and post-peak signal. The signal (S) is obtained by subtracting BG from TC; the noise (N) is calculated as the square root of BG. Therefore, the SNR for a peak of interest in XRF is calculated. It should be noted that this calculation method does not attempt to account for overlaps between peaks [24].

$$SNR = S / N = (TC - BG) / \sqrt{BG} \quad (3)$$

The number of channels used for the Cr peak area and also for the extraction of background counts were determined by inspection of the peak width for all liquid Cr solution measurements. In practice, due to the influence of electronic noise and statistical fluctuation of particles, the background noise was computed by averaging eight channels of the pre-peak and post-peak for all the liquid samples to minimize the uncertainty. In addition, the electronic noise associated mainly with the preamplifier and the electrical characteristics of the detector, introduce noise to the spectroscopy system. It is reflected on the spectrum by the width of the peaks. The Cr peak range is thus from 5.284 keV to 5.513 keV (75 channels) due to the imperfect energy resolution of the spectrometer. The spectrum from the purified water sample was subtracted from the spectra generated by the samples with Cr to suppress the background. It should be noted that to avoid negative background counts, the spectrum from the purified water was normalized by a factor of 0.5. Then the characteristic Cr photon counts in all measured spectra are integrated, respectively. For the MCNP simulation, a tally card, F8, was implemented, which is specific for detector pulse height determination. Thus, the detection process is simulated by using MCNP to obtain pulse height per emitted particle in the source, that is, absolute

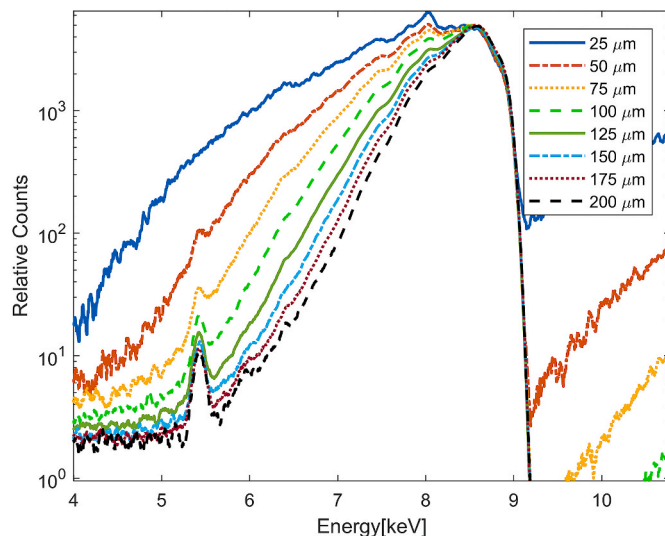


Fig. 3. Measured XRF spectra of Cr contaminated water (3.9 mg/L) with varying Cu filter thickness. With the filter thickness increasing, the visibility of the Cr peaks at 5.41 keV is increased.

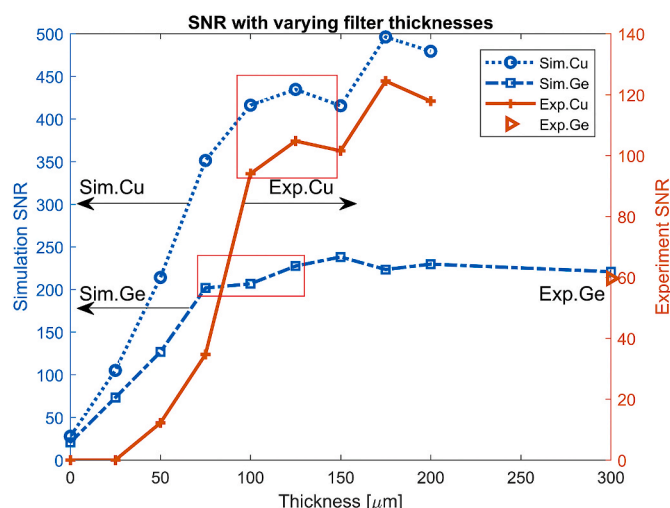


Fig. 4. The relationship between the SNR of the 3.9 mg/L Cr peak and various filter thicknesses (Cu and Ge filters).

efficiency for each spectrum peak in the source and for each modelled geometry. In this simulation, no attempt to account for the Gaussian energy broadening of the measured peaks in the spectrum is taken. Thus, the spectroscopy system is considered as being ideal, and the Cr signal is taken from the triangulation area at 5.400 keV in the simulation result. The triangle area depends on the peak height and on the setting for the simulation energy bin width. The MCNP code outputs a spectrum normalized to one photon. The normalization of the simulation data is necessary when comparing with experimental data [25]. The pulse area tally results were then normalized to a measured 3.9 mg/L Cr net peak for comparison to the measured data.

4. Results

4.1. Filter optimization with respect to signal-to-noise ratio

In order to estimate the effect of filter thickness to the spectrum, we measured the spectrum of a liquid sample with 3.9 mg/L of Cr with a set of Cu foils with various thicknesses, 25 μm , 50 μm , 75 μm , 100 μm , 125 μm , 150 μm , 175 μm and 200 μm . Depending on the filter thickness, which heavily influences the counting rate, the measurement time varies from 3 min up to 1 h. For comparison of the Cr peak, all measurements are normalized at 8.5 keV energy. Fig. 3 shows that the filter thickness has a significant influence on the passband range, resulting in different rising-edge. The Cr signal at 5.41 keV is located on the rising-edge of the energy window from the Cu filter. Due to the Compton scattering in the sample, the rising-edge shift towards to lower energy when comparing to the spectrum of a 100 μm Cu filter in Fig. 1. With a 25 μm Cu filter, the Cr peak is totally hidden in the background. The thickest Cu filter, 200 μm , allows a relatively low background noise level in the energy region at 5.41 keV, which reveals a clearly visible Cr peak. As the filter thickness increases, the energy windows becomes narrower and the visibility of the Cr peak improves. Those energy windows effectively suppresses the scattering background around 5.41 keV. Moreover, these spectra provide support about the selected energy ranges used in calculating SNR and LOQ. The SNRs for these Cr peak were further calculated and compared to the MCNP simulation.

The tendency of the SNR of the Cr peak versus filter thickness is shown in Fig. 4. Since the MCNP simulation describes an ideal situation, total noise in the simulation is much lower than in to the experiment. Hence a dual Y-axis is used in Fig. 4 when comparing the experimental and simulated SNR. The SNR is increased with the filter thickness increasing until a certain thickness, which shows an agreement with the spectra in Fig. 3. For thick filters, both the Cu filter and the Ge filter

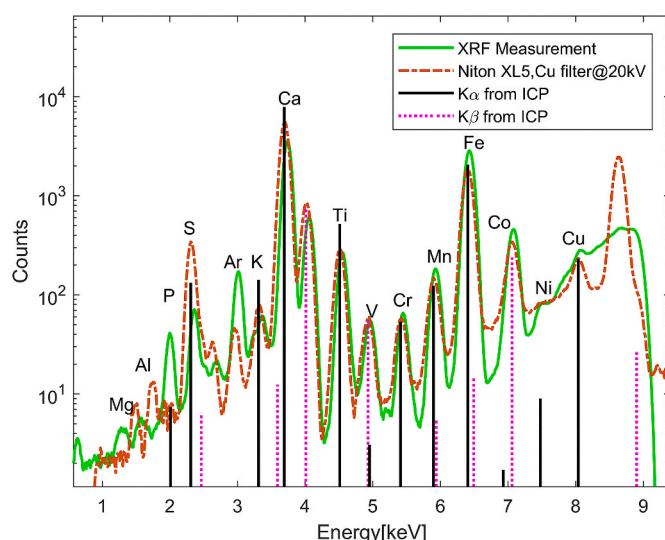


Fig. 5. A comparison of XRF spectra of ash sample obtained by our XRF setup using a 130 μm Cu filter and a commercial XRF with Cu filter. These are compared to ICP-MS measurements, which are converted to relative peak heights.

reached a saturated SNR value. For the Cu filter, there is no significant improvement in the SNR above 100 μm thickness. The SNR reaches approximately 100 in the measurement and 420 in the simulation at 100 μm , which is the best SNR we achieved in this study. The discrepancy between simulated and measured SNR with 25 μm and 0 μm filter is caused by radiation scattered by equipment holders etc. in the practical setup, which is not modelled in the simulation. For the Cu filter, the SNR tendency of the Cr peak from experiments shows a good agreement with simulations. Similarly, for the Ge filter thicknesses above 75 μm , the SNR reaches a saturation value of 200 in the simulation. One Ge filter/wafer with 300 μm thickness was measured in the experiment. The Cu filters achieve approximately two time higher SNR than the Ge filters in the plateau region. However, the intensity of the X-ray signal is exponentially decreased with increased thickness of the filter, thus the necessary measurement time is increased accordingly [26]. Hence, a tradeoff between high SNR and short measurement time should be considered when choosing filter material and thickness for a practical XRF setup [1]. The ideal filter is the combination of material and thickness that results in a minimum reduction of photon flux at useful high energies, but also maximum improvement of the SNR for a specific element. Thus, a Cu filter with 100–140 μm thickness or a Ge filter with 75–125 μm is a reasonable choice for optimizing the SNR of Cr.

4.2. XRF measurement for solid (ash sample)

In the solid fly ash measurement, a 130 μm thick Cu filter was chosen to optimize the SNR of the Cr peak. The measured spectrum of the fly ash from our setup (solid line) is compared with a commercial XRF measurement (dash-dot line) and ICP-MS measurement (solid and dotted bars) as shown in Fig. 5. The model of commercial XRF unit used is Niton XL5 [27], set to use a Cu filter and 20 kV tube voltage (the filter thickness of the Niton XRF device was not known by the authors). It should be noted that the Niton XL5 has a tighter geometry design, thus the angle between the X-ray tube and the detector is smaller than our setup. As aforementioned, this will cause a slight shift of continues X-ray spectrum due to the Compton scattering angle. The acquisition time for the Niton XL5 is 1 min. The reference spectra from the Niton XL5 were normalized for comparison to the measured data due to the different acquiring time. Moreover, the XRF spectrum must be quantified in order to compare it with the ICP-MS results.

The $K\alpha$ peak of Cr is clearly visible in the XRF spectra in the fly ash

Table 4

Major element content measured by XRF, commercial XRF, and ICP-MS (Unit: mg/kg).

	Ca	Fe	K	Mn	Ti	Cr	S
XRF	78158	27920	2130	1899	4388	659	51467
XRF Niton	164158 ± 520	14250 ± 110	3254 ± 130	1017 ± 40	4216 ± 50	369 ± 10	77301 ± 690
ICP-MS	189000 ± 32000	20200 ± 3800	4904 ± 970	1360 ± 200	8630 ± 1600	651 ± 120	95900 ^a

^a The analysis is not accredited.

sample. Apart from Cr, the spectra resolve peaks from a lot of elements, such as Sulfur (S), Potassium (K), Calcium (Ca), Titanium (Ti), Manganese (Mn), Iron (Fe), and Nickel (Ni). When the sample contains several elements, the peaks might overlap with other elements resulting in false XRF readings. As an example, the Vanadium (V) K β peak at 5.42 keV merges with the Cr peak at 5.41 keV. However, in the ICP measurement, the V content is much lower than the Cr content and the relative intensity of K β is low compared to K α in V. Thus, the contribution of V K β is neglectable compared to Cr K α . Moreover, the K β peak of Cr at 5.94 keV overlaps with the K α peak of Mn at 5.90 keV, while the peak present at 5.41 keV is able to identify Cr. According to Table 1, the relative intensity ratio of the K β peak of Cr to the K α peak of Cr is 1:10. Assuming all the photons at 5.41 keV is contributed by the Cr in the sample, by using the relative intensity ratio, we calculate that the fluorescence photons from Cr contribute 3.75% to the overlapping peak at 5.90 keV in this measurement. It should be noted that escape peaks arise when a strong element peak is recorded. The strong Ca peak at 3.69 keV gives rise to an escape peak at 1.95 keV when Si fluorescence photons at 1.74 keV escape the detector. This escape peak is merged with the K α peak of P at 2.01 keV. The Argon (Ar) peaks present in the spectra at 2.96 keV and 3.19 keV are due to the normal atmosphere content of Ar since no Argon is expected in the ash. Magnesium (Mg), Aluminum (Al) and Phosphorus (P) are not included in the soil calibration of the commercial instrument. These lighter elements are outside the focus of interest of this specific measurement application. The XRF measurements identify all key elements expected in the ICP-MS analysis, if the fluorescence energy is between 2 keV and 8 keV. In order to detect a lighter element that has fluorescence energies below 2 keV with XRF, the absorption in air must be considered, which depends upon the distance between the sample and the detector and the photon energy. Mg and Al shows very low readings in the ICP-MS analysis, and the XRF peaks of Mg at 1.25 keV and Al at 1.49 keV originate either from the source spectrum or from the materials in the equipment.

A simplified conversion between the concentration in ppm and the fluorescence peak intensity considers the fluorescence yield ω , the X-ray attenuation coefficient in air (A_C), the relative intensity of each line (Rel_{int}), and the atomic weight (m) for each element, as shown in Equation (4). The *Peak Intensity* is the peak value of a specific element and N is a normalization factor. It should be noted that the setup and the normalization is optimized for Cr measurements. This relationship does not consider the influence of sample thickness, density or matrix effects.

$$ppm = N \cdot m \cdot \text{Peak Intensity} / (\omega \cdot A_C \cdot Rel_{int}) \quad (4)$$

In Table 4, the main elements from our XRF setup are compared with ICP-MS analysis values and commercial XRF readings using a Niton XL5 device with soil calibration. Compared to the chemical analysis, both XRF measurements underestimate the concentration of K, Ti and S. The commercial device shows a 44% lower Cr value when compared with the ICP-MS value. Although our setup is optimized for Cr detection, the other elements also show a reasonable agreement with ICP-MS and commercial XRF readings. The high readings achieved for Fe and Mn might be due to that the normalization factor is optimized for Cr. Fe contributions might also come from setup materials like the optic table. The lower concentration of Ca in the XRF measurement is due to the escape peak from the detector, which is compensated for in the calibration of the commercial device. In addition, the differences in setup geometry between the commercial device and the developed device

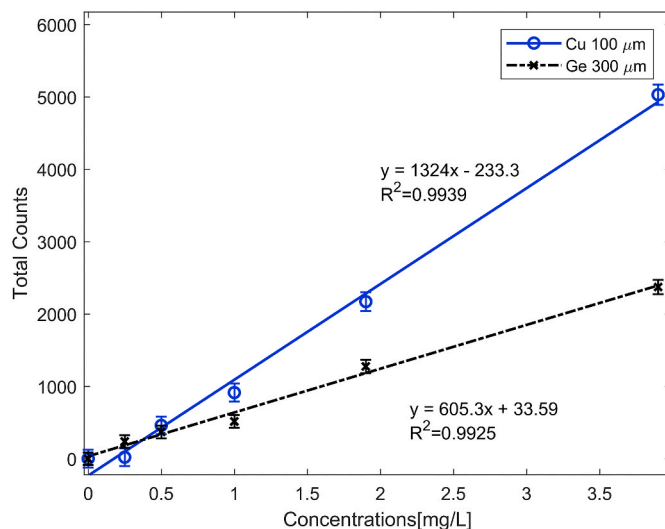


Fig. 6. Calibration curve for Cr XRF measurements using a 100 μm Cu filter and a 300 μm Ge filter. The error bars indicate the statistical error.

affects the output spectrum. Since fly ash is an inhomogeneous material and the raw sample is not grinded, different XRF measurements will differ slightly from each other. Although our system is optimized for liquid samples, the discussed comparison verifies the reliability of our measurement for a dry complex sample. The statistical error of each measurement is displayed in Table 4. Note however that the actual XRF deviation is not only due to statistics, but also due to systematic errors related to the calibration for the XRF system. This is further discussed in the Matrix Effect section in the discussion chapter. The error intervals corresponds to a 95% confidence interval.

4.3. XRF measurements for liquids (leachate sample)

To achieve a higher beam intensity, a 100 μm Cu filter was used to optimize the Cr contamination measurement in liquid samples. Measurements with a 300 μm Ge filter were also performed. This Ge filter thickness is not optimal concerning exposure time, but it was an available filter and it gives a saturated SNR according to Fig. 4. Six calibration samples were used with Cr concentration of 3.9 mg/L, 1.9 mg/L, 1 mg/L, 0.5 mg/L, 0.25 mg/L and 0 mg/L. These samples are compared with one landfill leachate sample. In the XRF measurements, the fluorescence intensity of the Cr is not only correlated with the concentration but also normalized with the X-ray intensity after the filter. Since the energy range and the total counts within the energy window of the Cu filter and the Ge filter differs, by using a ratio, we can offset the influence of the filter or the measurement time. Thus, the 300 μm Ge is normalized by a factor 1.13, which is the total counts ratio of 100 μm Cu source filter and 300 μm Ge for purified water measurement.

For 3.9 mg/L Cr solution, the energy resolution for Cr peak at 5.41 keV is approximate 3.3% with a Cu filter and 2.8% with a Ge filter. The Cr signals from the known samples decrease following the decrease in the Cr concentration in both measurements, as expected. In quantitative XRF analysis, the measured fluorescent intensities are proportional to the concentration of the analytes. In order to obtain the calibration

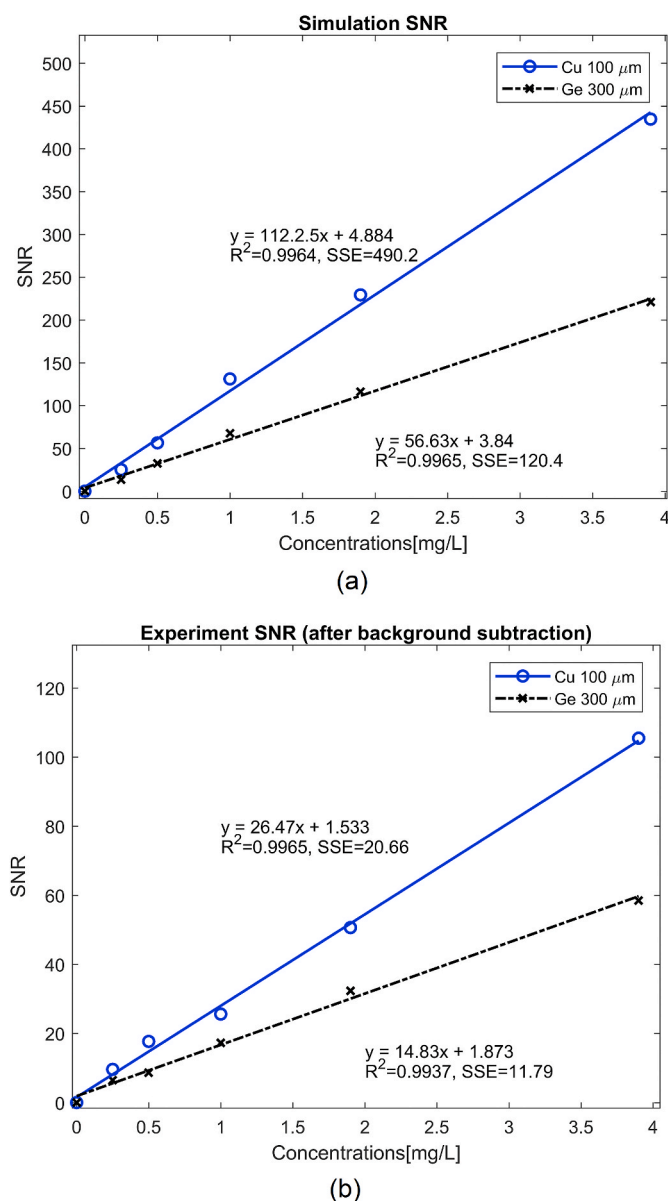


Fig. 7. (a) Simulation SNR curve for Cr solution with various concentrations using a 100 μm Cu filter and a 300 μm Ge filter. (b) Experiment SNR curve for Cr solution with various concentrations using a 100 μm Cu filter and a 300 μm Ge filter.

curve for Cr, the characteristic Cr photon counts in all measured spectra are integrated, respectively. A least-squares fit was applied to these data. The relationship between the concentration of Cr and the total counts of the Cr peaks with a 100 μm Cu filter and a 300 μm Ge filter is given in Fig. 6. The error bars shows the standard deviation of the net counts that is deduced from the quadrature sum of the total counts and the background counts [28]. By using the calibration curve, this setup can be used to predicate the Cr concentration of unknown liquid samples. In practice, the range of our calibration focuses to cover the region close to limit for allowed concentrations in leachate. The calibration might not be valid for high Cr concentrations.

5. Discussion

5.1. Limit of quantitation

The SNR calculation of Cr provides an objective method in the

Table 5

SNR values and LOQ of Cr in liquid.

SNR	0.25 mg/L	0.5 mg/L	1 mg/L	1.9 mg/L	3.9 mg/L	LOQ (mg/L)
Exp.Cu (A)	9.60	17.70	25.61	50.65	105.48	0.32
Exp.Ge (B)	6.43	8.66	17.31	32.34	58.44	0.55
A/B	1.49	2.06	1.48	1.57	1.80	NULL
Sim.Cu (C)	25.13	56.46	131.12	229.30	434.61	0.05
Sim.Ge (D)	13.57	32.58	67.49	116.12	220.86	0.11
C/D	1.85	1.73	1.94	1.97	1.97	NULL

calculation of LOQ, the smallest quantity of analyte that can be measured with 'acceptable' accuracy and precision. The calculated LOQ can be used for XRF performance evaluation. A commonly accepted definition of LOQ is when the concentration of an element is greater than $\text{SNR} \geq 10$, which means that the characteristic peak of an element at a concentration is greater than the background by a statistically significant amount [2]. Fig. 7 presents SNR curves for Cr solutions with various concentrations using a 100 μm Cu filter and a 300 μm Ge filter in the MCNP simulations and in the experiments. The linearity of the SNR is proportional to the Cr concentrations. Table 5 displays the SNR and LOQ of Cr in liquid in the MCNP simulation and in the experiment. For the same Cr concentration, the SNR for the Cu filter is approximately twice that for the Ge filter. Due to less noise in the simulation, the LOQ is regarded as an ideal case and is much lower than for the experiment. We identified that 0.32 mg/L (Cu) and 0.55 mg/L (Ge) is the limit of quantitation for this system, which is well below the leachate allowed standard for Cr contamination (2.5 mg/L) in Sweden [29]. When an analytic concentration is near the detection limit, the uncertainty for that measurement is large. In the ICP-MS measurement, the concentration of the Cr in the leachate is 0.05 mg/L. The predicted Cr concentration in the leachate is 0.18 mg/L with Cu calibration and 0.25 mg/L with Ge calibration, which seems beyond the limit of quantitation in this XRF setup.

A simple adjustment to improve LOQ during the calibration phase is to increase the counting time. This improvement occurs because the signal varies linearly with counting time, whereas the noise varies with the square root of counting time as shown in Equation (3). Thus, for every doubling of the counting time, the SNR and LOQ would theoretically improve by a factor of $\sqrt{2}$. For the calibrations in this study, the counting time for all liquid samples is 2 h, which is considered as reasonable exposure time to suppress the statistical influence of the SNR. Measurement of concentrations close to or below LOQ might need longer measurement times compared to high concentrations. For longer counting times, evaporation and layering of the liquid samples should be considered, which might cause changes in the concentration. Furthermore, the counting time can be reduced by applying an X-ray source with higher beam intensity. For heavier elements, the LOQ would improve with the increase of fluorescence yields. However, the SNR and LOQ is also strongly affected by the scattered signal from the surroundings and the unfiltered signal from the source in XRF analysis. The authors in Refs. [30,31] studied the sources of error in sample preparation for XRF analysis. In quantitative XRF analysis, the presence of counting statistical errors due to the random fluctuations associated to the process of measurement of X-ray peak intensities, can be considered as a measure of the repeatability [32]. When implementing this method for liquid samples, a decision about required LOQ and recommended measurement times must consider the repeatability of the method. For optimizing heavier elements such as Arsenic, Cadmium, etc., the X-ray filter, the tube voltage [24] and the exposure time [33] need to be adjusted.

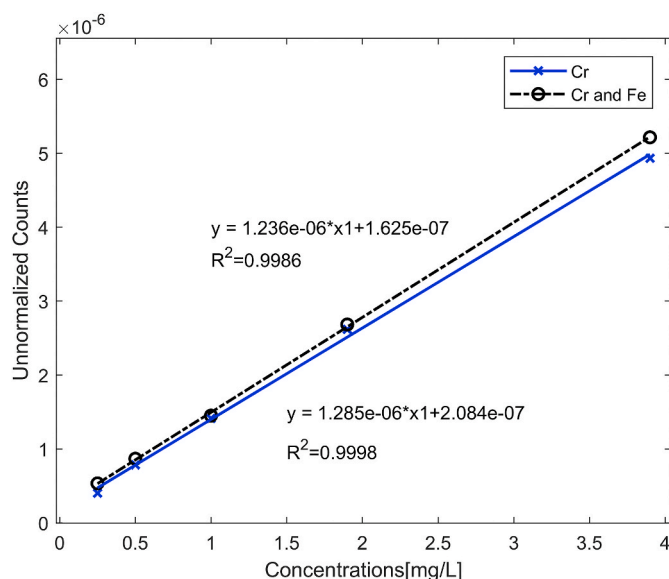


Fig. 8. Matrix effect of Fe-Cr in MCNP simulations. The presence of Fe in the sample enhanced the Cr peak heights.

Table 6

Matrix effect between Fe and varying concentration of Cr.

Sample	0.25 mg/L	0.5 mg/L	1 mg/L	1.9 mg/L	3.9 mg/L
Cr and Fe (E)	5.33e-7	8.66 e-7	1.45 e-6	2.68 e-6	5.21 e-6
Cr (F)	3.99 e-7	7.83 e-7	1.41 e-6	2.62 e-6	4.93 e-6
E/F (%)	133	110	103	102	106

5.2. Matrix effects

X-ray fluorescence is subject to significant matrix effects, which must be considered in order to obtain accurate quantitative results. These are due to both absorption and enhancement effects, which affects the magnitude of the analyte signal [34]. A study on the influence of matrix effects in XRF with samples of two elements of Fe–Cr was carried out in MCNP simulation. A 100 μm Cu filter was applied to suppress the background scattering and a high Fe concentration (6.1 mg/L) was expected in this landfill leachate. The matrix effect of a fixed Fe concentration and varying Cr concentration is shown in Fig. 8. The emitted Fe line at 6.4 keV enhanced the excitation of Cr atoms. The Cr peak value are listed in Table 6. This enhancement effect from 6.1 mg/L Fe would overestimate the Cr contamination with 2%–6% at 2.5 mg/L, which is the allowed concentration in Sweden. The two most efficient mathematical methods for the correction of matrix effects: influence coefficients and fundamental parameters, and their application has been discussed in Ref. [35]. Our study shows that the influence of Fe is more obvious for low concentration Cr sample in an XRF system. The enhancement effect can be up to 33% for a 0.25 mg/L Cr solution. Hence, the matrix effect must be carefully corrected for when detecting trace elements using an XRF system.

6. Conclusions and future works

In this work, direct XRF analysis has been demonstrated to detect Cr contamination in ash and leachate. The signal-to-noise ratio was improved by optimizing the X-ray filter, allowing the possibility of Cr assessment at relatively low concentrations. By adjusting the X-ray filter thickness, the detection limit can be enhanced significantly for detecting Cr. Properly selecting the filter material and thickness is critically important for reducing background and thus improving detection limits for a given set of elements. For detecting Cr, a Cu filter with a thickness

between 100 μm and 140 μm is recommended when considering the tradeoff between SNR and measurement time for a practical XRF setup.

This system can be used to detect Cr for monitoring of environmental limits in leachate on-line, on-site, if designed and calibrated properly. Since high Fe concentration is expected in the leachate, the matrix effect can lead to slight over-prediction of the Cr content. The further process to correct for the matrix effect giving rise to summing of peaks, and to correct for escape peaks from the detector material, must be considered for an accurate system. For optimizing this setup for other hazardous elements with higher atomic number, the X-ray filter, the tube voltage and the exposure time need to be adjusted. How to estimate a shortest measurement time that still provides reasonable statistics could be future work. Another study could be if it is possible to achieve smoothed background measurement providing higher accuracy after background subtraction.

Credit author statement

Siwen An: Methodology, Software, Validation, Formal analysis, Investigation, Data curation Management, Writing – Original/Revised Draft. Salim Reza: Formal analysis, Resources, Writing – review & editing. Börje Norlin: Conceptualization, Resources, Supervision, Project administration, Writing – review & editing, Funding acquisition. Christer Fröjd: Conceptualization, Writing – review & editing. Göran Thungström: Conceptualization, Writing – review & editing.

Declaration of competing interest

The authors declare that they have no known competing financial interests or personal relationships that could have appeared to influence the work reported in this paper.

Acknowledgments

We thank Sara Norström and Ana-Paola Vilches at Mid Sweden University for performing the ICP measurements and analysis of leachate samples and for assistance with ICP report for fly ash measurements provided by Statens Geotekniska Institute. We would also like to show our gratitude to the Liselott Granlund at Holger Andreassen AB for sharing their commercial Niton XL5 instrument. The authors are grateful to the City of Sundsvall and the EU Regional Development Fund for their support, and to Cecilia Bjarnhagen and Anette Rhodin at Sundsvall Energi Korstaverket for providing ash samples and relevant knowledge.

References

- [1] S. An, B. Norlin, M. Hummelgård, G. Thungström, Comparison of elemental analysis techniques for fly ash from municipal solid waste incineration using X-rays and electron beams, *IOP Conf. Ser. Earth Environ. Sci.* 337 (2019) 12007, <https://doi.org/10.1088/1755-1315/337/1/012007>.
- [2] S.M. Raghab, A.M. Abd El Meguid, H.A. Hegazi, Treatment of leachate from municipal solid waste landfill, *HBRC J* 9 (2013) 187–192, <https://doi.org/10.1016/j.hbrj.2013.05.007>.
- [3] S.A. Katz, H. Salem, The toxicology of chromium with respect to its chemical speciation: a review, *J. Appl. Toxicol.* 13 (1993) 217–224, <https://doi.org/10.1002/jat.2550130314>.
- [4] T.L. Rinehart, D.G. Schulze, R.M. Bricka, S. Bajt, E.R. Blatchley, Chromium leaching vs. oxidation state for a contaminated solidified/stabilized soil, *J. Hazard Mater.* 52 (1997) 213–221, [https://doi.org/10.1016/S0304-3894\(96\)01808-0](https://doi.org/10.1016/S0304-3894(96)01808-0).
- [5] Z. Sun, P. Liang, Determination of Cr(III) and total chromium in water samples by cloud point extraction and flame atomic absorption spectrometry, *Microchim. Acta.* 162 (2008) 121–125, <https://doi.org/10.1007/s00604-007-0942-0>.
- [6] A.D. Apte, V. Tare, P. Bose, Extent of oxidation of Cr(III) to Cr(VI) under various conditions pertaining to natural environment, *J. Hazard Mater.* 128 (2006) 164–174, <https://doi.org/10.1016/j.jhazmat.2005.07.057>.
- [7] S. Iwata, K. Chiba, H. Haraguchi, E. Fujimori, K. Minamoto, Enrichment of elements in industrial waste incineration bottom ashes obtained from three different types of incinerators, as studied by ICP-AES and ICP-MS, *J. Mater. Cycles Waste Manag.* 6 (2004) 73–79, <https://doi.org/10.1007/s10163-003-0106-6>.
- [8] N. Panichev, K. Mandiwana, M. Kataeva, S. Siebert, Determination of Cr(VI) in plants by electrothermal atomic absorption spectrometry after leaching with

- sodium carbonate, in: *Spectrochim. Acta - Part B at. Spectrosc.*, Elsevier, 2005, pp. 699–703, <https://doi.org/10.1016/j.sab.2005.02.018>.
- [9] A. Rajib, A. Saiful Islam, M. Razu Ahmed, M. Tariqur Rahman, M. Atowar Rahman, A.B. Md Ismail, Detection of chromium (Cr) using X-ray fluorescence technique and investigation of Cr propagation from poultry feeds to egg and chicken flesh, *Am. J. Eng. Res.* 5 (2016) 243–247, www.ajer.org. (Accessed 5 August 2020).
- [10] V. Orescanin, L. Mikelic, S. Lulic, M. Rubcic, Determination of Cr(III) and Cr(VI) in industrial and environmental liquid samples by EDXRF method, *Anal. Chim. Acta* 527 (2004) 125–129, <https://doi.org/10.1016/j.aca.2004.09.027>.
- [11] S. Reza, H. Chang, B. Norlin, C. Frojdh, G. Thungstrom, Detecting Cr contamination in water using X-ray fluorescence, in: 2015 IEEE Nucl. Sci. Symp. Med. Imaging Conf. NSS/MIC 2015, Institute of Electrical and Electronics Engineers Inc., 2016, <https://doi.org/10.1109/NSSMIC.2015.7581750>.
- [12] R. Schlotz, S. Uhlig, Introduction to X-Ray Fluorescence (XRF). User's Manual. (Bruker Advanced X-Ray Solutions: Karlsruhe), 2002. www.bruker-axs.com. (Accessed 5 August 2020).
- [13] A.N. Kadachi, M.A. Al-Eshaikh, Limits of detection in XRF spectroscopy, *X Ray Spectrom.* 41 (2012) 350–354, <https://doi.org/10.1002/xrs.2412>.
- [14] D. Pearson, S. Chakraborty, B. Duda, B. Li, D.C. Weindorf, S. Deb, E. Brevik, D. P. Ray, Water analysis via portable X-ray fluorescence spectrometry, *J. Hydrol.* 544 (2017) 172–179, <https://doi.org/10.1016/j.jhydrol.2016.11.018>.
- [15] IAEA TECDOC Series, Sampling, Storage and Sample Preparation Procedures for X Ray Fluorescence Analysis of Environmental Materials, IAEA, 1997.
- [16] T. Moriyama, A. Morikawa, Sample preparation for X-ray fluorescence analysis VII. Liquid sample, *Rig J* 33 (2017) 24–29, <https://www.rigaku.com/journal/winter-2017-volume-33-no-1/24-29>. (Accessed 5 August 2020).
- [17] P.R. Aranda, S. Moyano, L.D. Martinez, I.E. De Vito, Determination of trace chromium(VI) in drinking water using X-ray fluorescence spectrometry after solid-phase extraction, *Anal. Bioanal. Chem.* 398 (2010) 1043–1048, <https://doi.org/10.1007/s00216-010-3950-y>.
- [18] C.J. Werner, MCNP User's Manual Code Version 6.2, Los Alamos, 2017. https://mcnp.lanl.gov/mcnp_manual.shtml. (Accessed 5 August 2020).
- [19] X.- Ray, Data booklet, n.d. <https://xdb.lbl.gov/>. (Accessed 5 August 2020).
- [20] René E. Van Grieken, *Handbook of X-Ray Spectrometry*, Marcel Dekker Inc, New York, 2001, pp. 199–236.
- [21] X-ray sources | moxtek, n.d. <https://moxtek.com/x-ray-products/x-ray-sources/>. (Accessed 5 August 2020).
- [22] X-123SDD complete X-ray spectrometer with silicon drift detector (SDD) – amptek – X-ray detectors and electronics, n.d. <https://www.amptek.com/products/sdd-x-ray-detectors-for-xrf-eds/x-123sdd-complete-x-ray-spectrometer-with-silicon-drift-detector-sdd#Specifications>. (Accessed 5 August 2020).
- [23] T. Ernst, T. Berman, J. Buscaglia, T. Eckert-Lumsdon, C. Hanlon, K. Olsson, C. Palenik, S. Ryland, T. Trejos, M. Valadez, J.R. Almirall, Signal-to-noise ratios in forensic glass analysis by micro X-ray fluorescence spectrometry, *X Ray Spectrom.* 43 (2014) 13–21, <https://doi.org/10.1002/xrs.2437>.
- [24] A.F. Jones, J.N. Turner, J.S. Daly, P. Francus, R.J. Edwards, Signal-to-noise ratios, instrument parameters and repeatability of Itrax XRF core scan measurements of floodplain sediments, *Quat. Int.* 514 (2019) 44–54, <https://doi.org/10.1016/j.quaint.2018.09.006>.
- [25] A.J. Specht, M.G. Weisskopf, L.H. Nie, Theoretical modeling of a portable x-ray tube based KXRF system to measure lead in bone, *Physiol. Meas.* 38 (2017), <https://doi.org/10.1088/1361-6579/aa5efe>.
- [26] J.H. Hubbell, Photon Cross Sections, Attenuation Coefficients, and Energy Absorption Coefficients from 10 keV to 100 GeV, Washington DC, 1969, <https://doi.org/10.6028/NBS.NSRDS.29>.
- [27] NitonTM XL5 handheld XRF analyzer, n.d. <https://www.thermofisher.com/order/catalog/product/NITONXL5?SID=srch-srp-NITONXL5#/NITONXL5?SID=srch-srp-NITONXL5>. (Accessed 5 August 2020).
- [28] G.F. Knoll, *Radiation Detection and Measurement*, third ed., John Wiley & Sons, 2010, pp. 83–88, <https://doi.org/10.4274/nts.2017.018>.
- [29] Handbook, The Swedish Environmental Protection Agency's Regulations on Landfilling, Criteria and Procedures for Receiving Waste at Facilities for Landfilling Waste, Stockholm, 2004. <http://www.naturvardsverket.se/Documents/publikationer/620-0144-2.pdf?pid=2569>.
- [30] N. Krusberski, Exploring Potential Errors in XRF Analysis, 2006. <http://saimm.org.za/Conferences/AnalyticalChallenges/11-Krusberski.pdf>. (Accessed 18 August 2020).
- [31] D. Coler, L. Bruzenak, I. Campbell, C. Republic, The common sources of error in sample preparation for XRF analysis and the capabilities of standalone automation, n.d. https://cdn2.hubspot.net/hubfs/494827/AAACaseStoryPDF/Common_sources_of_error_in_sample_preparation_for_XRF_Analysis_and_the_Capabilities_of_Standalone_Automation.pdf. (Accessed 18 August 2020).
- [32] R.M. Rousseau, Detection limit and estimate of uncertainty of analytical XRF results, *Rig J* 18 (2001) 33–47, https://www.researchgate.net/publication/228687395_Detection_limit_and_estimate_of_uncertainty_of_analytical_XRF_results. (Accessed 5 August 2020).
- [33] J.-J. Huang, L. Löwemark, Q. Chang, T.-Y. Lin, H.-F. Chen, S.-R. Song, K.-Y. Wei, Choosing optimal exposure times for XRF core-scanning: suggestions based on the analysis of geological reference materials, *G-cubed* 17 (2016) 1558–1566, <https://doi.org/10.1002/2016GC006256>.
- [34] R. Sitko, B. Zawisz, Quantification in X-ray fluorescence spectrometry, in: *X-Ray Spectrosc. InTech*, 2012, pp. 142–143, <https://doi.org/10.5772/29367>.
- [35] R.M. Rousseau, Corrections for matrix effects in X-ray fluorescence analysis-A tutorial, *Spectrochim. Acta Part B At. Spectrosc.* 61 (2006) 759–777, <https://doi.org/10.1016/j.sab.2006.06.014>.